

Spitzer Point-Source Catalogs of $\sim 300,000$ Stars in Seven Nearby Galaxies¹

Rubab Khan^{2,3}, K. Z. Stanek^{4,5}, C. S. Kochanek^{4,5}, G. Sonneborn³

ABSTRACT

We present *Spitzer* IRAC $3.6\text{--}8\,\mu\text{m}$ and MIPS $24\,\mu\text{m}$ point-source catalogs for seven galaxies: NGC 6822, M 33, NGC 300, NGC 2403, M 81, NGC 0247, and NGC 7793. The catalogs contain a total of $\sim 300,000$ sources and were created by dual-band selection of sources with $> 3\sigma$ detections at both $3.6\,\mu\text{m}$ and $4.5\,\mu\text{m}$. The source lists become significantly incomplete near $m_{3.6} = m_{4.5} \simeq 18$. We complement the $3.6\,\mu\text{m}$ and $4.5\,\mu\text{m}$ fluxes with $5.8\,\mu\text{m}$, $8.0\,\mu\text{m}$ and $24\,\mu\text{m}$ fluxes or 3σ upper limits using a combination of PSF and aperture photometry. This catalog is a resource as an archive for studying mid-infrared transients and for planning observations with the James Webb Space Telescope.

Subject headings: — catalogs — surveys — techniques: photometric — infrared: stars — galaxies: individual (NGC 6822, M 33, NGC 300, NGC 2403, M 81, NGC 0247, and NGC 7793)

1. Introduction

The *Spitzer* Space Telescope (*Spitzer*, Werner et al. 2004) enabled mid-infrared (mid-IR) observations with unprecedented sensitivity. An enormous archive of imaging data has been collected using the Infrared Array Camera (IRAC, Fazio et al. 2004) and the Multiband Imaging Photometer (MIPS, Rieke et al. 2004) instruments aboard *Spitzer* that have been utilized to study astrophysical objects in the Galaxy (e.g., Benjamin et al. 2003) and beyond. In particular, *Spitzer* made it possible to study resolved stellar populations in the Magellanic Clouds (Meixner et al. 2006; Bolatto et al. 2007; Gordon et al. 2011) and local group galaxies such as M 31 (Barmby et al. 2006; Mould et al. 2008) and M 33 (McQuinn et al. 2007; Thompson et al. 2009) in the mid-IR.

¹Based on observations made with the *Spitzer* Space Telescope, which is operated by the Jet Propulsion Laboratory, California Institute of Technology under a contract with NASA.

²JWST Fellow, NASA Postdoctoral Program, ORAU, P.O. Box 117, MS 36, Oak Ridge, TN 37831

³NASA Goddard Space Flight Center, MC 665, 8800 Greenbelt Road, Greenbelt, MD 20771; rubab.m.khan, george.sonneborn-1@nasa.gov

⁴Dept. of Astronomy, The Ohio State University, 140 W. 18th Ave., Columbus, OH 43210; kstanek, ckochanek@astronomy.ohio-state.edu

⁵Center for Cosmology and AstroParticle Physics, The Ohio State University, 191 W. Woodruff Ave., Columbus, OH 43210

Although global galaxy properties beyond the local group have been extensively studied using *Spitzer* images (Kennicutt et al. 2003; Dale et al. 2009; Sheth et al. 2008), efforts to catalog individual mid-IR luminous sources in these galaxies have been limited. There are a number of sources of archival *Spitzer* data for nearby galaxies. The *Spitzer* Infrared Nearby Galaxies Survey (SINGS, Kennicutt et al. 2003) made a comprehensive mid-IR imaging and spectroscopic survey of 75 galaxies, many of them within 10 Mpc. The Local Volume Legacy Survey (LVL, Dale et al. 2009) surveyed a total of 256 nearby galaxies, including all known galaxies inside a sub-volume bounded by 3.5 Mpc and an unbiased sample of S-Irr galaxies within a larger, and more representative, 11 Mpc sphere. The *Spitzer* Survey of Stellar Structure in Galaxies (*S⁴G*, Sheth et al. 2008) collected data for ~ 2300 galaxies within 40 Mpc using the warm *Spitzer* ($3.6\ \mu\text{m}$ and $4.5\ \mu\text{m}$) bands.

While it is difficult to identify and characterize mid-IR point sources in the crowded and dusty disks of large star forming galaxies due to IR emission from interstellar dust, blending and background contamination, it is nonetheless feasible to identify and photometer mid-IR luminous stars in galaxies well beyond the Magellanic clouds (Thompson et al. 2009; Khan et al. 2010, 2011; Gerke & Kochanek 2013). In Khan et al. (2013), we used archival IRAC images of seven galaxies ($\lesssim 4$ Mpc; closest to farthest: NGC 6822, M 33, NGC 300 (see Helou et al. 2004), NGC 2403, M 81 (see Willner et al. 2004), NGC 0247, and NGC 7793) in a pilot study to search for extragalactic analogs of the Galactic object η Carinae, taking advantage of the data made available by the SINGS and LVL projects, which led to the identification of an emerging class of evolved massive ($M \simeq 25 \sim 60\ M_{\odot}$) stars (Khan et al. 2015).

Here we present photometric inventories of the mid-IR point sources in the IRAC $3.6\ \mu\text{m}$, $4.5\ \mu\text{m}$, $5.8\ \mu\text{m}$, $8\ \mu\text{m}$ and MIPS $24\ \mu\text{m}$ images of the galaxies studied by Khan et al. (2013, 2015). Although we concentrated on galaxies with recent star formation, as only these would have large numbers of the short lived, very massive stars that were our primary targets, we also included the small, low-mass galaxy NGC 6822 as a test for examining large numbers of smaller, lower-metallicity systems. M 33 ($D \simeq 0.96$ Mpc, Bonanos et al. 2006) was previously cataloged by McQuinn et al. (2007) in the IRAC 3.6 , 4.5 and $8.0\ \mu\text{m}$ bands, and by Thompson et al. (2009) in the IRAC 3.6 and $4.5\ \mu\text{m}$ bands. Point sources in NGC 300 ($D \simeq 1.9$ Mpc, Gieren et al. 2005) and M 81 ($D \simeq 3.6$ Mpc, Gerke et al. 2011) were cataloged by Khan et al. (2010) in the IRAC 3.6 and $4.5\ \mu\text{m}$ bands. The catalogs presented in this paper identify a larger number of sources in these galaxies than the previous studies. *Spitzer* point-source catalogs of NGC 6822 ($D \simeq 0.46$ Mpc, Gieren et al. 2006), NGC 2403 ($D \simeq 3.1$ Mpc, Saha et al. 2006), NGC 0247 ($D \simeq 3.6$ Mpc, Madore et al. 2009) and NGC 7793 ($D \simeq 4.1$ Mpc, Tully et al. 2009) are being published here for the first time.

We use the same mosaics that were utilized by Khan et al. (2013, 2015). For M 33, we use the six co-added epochs of IRAC images from McQuinn et al. (2007) that was originally created and used by Thompson et al. (2009), and the MIPS data retrieved from the *Spitzer Heritage Archive*⁶. For NGC 300 and NGC 247, we used the mosaics from the LVL survey (Dale et al.

⁶<http://sha.ipac.caltech.edu/applications/Spitzer/SHA/>

2009). For NGC 6822, NGC 2403, M 81, and NGC 7793, we used the mosaics from the SINGS survey (Kennicutt et al. 2003). We utilize the full mosaics available for each galaxy. Figure 1 shows the IRAC 3.6 μm images of the targeted galaxies. In what follows, we describe our methodology (Section 2) and present the point-source catalogs (Section 3).

2. Photometry

In this Section, we detail how we obtained the photometric measurements at various wavelengths and combined them to construct the point-source catalogs. Although the procedures followed here are derived from the techniques developed by Khan et al. (2010) and Khan et al. (2013), there are some key differences, as we now carry out an inventory of all point sources rather than targeting a particular sub class with desired photometric properties.

Specifically, Khan et al. (2010) searched for very red mid-IR ($m_{3.6} - m_{4.5} > 1.5$) sources near or at the detection limit of the first two IRAC bands, and therefore included in their primary source-list objects that were detected in the 4.5 μm but not the 3.6 μm image, as well as objects that could only be detected in the 4.5 $\mu\text{m} - 3.6 \mu\text{m}$ difference image but not in either of the individual images. Khan et al. (2013) focused on the most luminous mid-IR ($L_{\text{mid-IR}} > 10^5 L_{\odot}$) sources with a spectral energy distribution (SED) that is either flat across the four IRAC bands or rising towards the longer wavelengths, and therefore included in the primary source list all objects that had $\lambda L_{\lambda} > 10^4 L_{\odot}$ in any of the first three (3.6 μm , 4.5 μm , 5.8 μm) IRAC bands.

In this work, we implement strict detection criteria by selecting all sources detected at $> 3\sigma$ in both the 3.6 μm and 4.5 μm images within a certain matching radius as point sources. Next, we search for $> 3\sigma$ detections of these point sources in the 5.8 μm and 8.0 μm images within the same matching radius. If no counterpart is found, we attempt to measure the flux at the location of the 3.6/4.5 μm point source through PSF fitting, and failing that, through aperture photometry. For the MIPS 24 μm images, we only use aperture photometry due to the much lower resolution and larger PSF size compared to the IRAC images. Finally, for all objects that do not have a $> 3\sigma$ detection at 5.8 μm , 8.0 μm and 24 μm , we estimate the 3σ flux upper limits. The fluxes and upper limits are transformed to Vega-calibrated magnitudes using the flux zero points⁷ and aperture corrections provided in the *Spitzer* Data Analysis Cookbook⁸. Given this broad outline, we now describe the specific technical details of how we performed the measurements at the various stages of constructing the catalogs.

We used the DAOPHOT/ALLSTAR PSF-fitting and photometry package (Stetson 1992) to construct the PSFs, to identify the $> 3\sigma$ sources, and to measure their flux at all 4 IRAC bands. The different roll angles of the various *Spitzer* observations made it necessary to construct the PSFs

⁷280.9, 179.7, 115.0, 64.13 and 7.17 Jy for 3.6, 4.5, 5.8, 8.0 and 24 μm bands.

⁸<http://irsa.ipac.caltech.edu/data/SPITZER/docs/dataanalysisistools/>

for each galaxy in each band independently. Next, we empirically determined the optimal radius to match the $3.6\,\mu\text{m}$ and $4.5\,\mu\text{m}$ source lists. Figure 2 shows the distribution of distances to the nearest $3.6\,\mu\text{m}$ source for each $4.5\,\mu\text{m}$ source in M 33. In this case, over 90% have a match within 0.5 pixel. The density of nearest matches falls rapidly between $0.5 - 1.0$ pixel ($< 10\%$ additional matches), while the number of duplicates increases ($< 0.5\%$ duplicate matches), and then the distribution essentially flattens. Similar distributions are observed for the other six galaxies (see Table 1). We therefore adopted an empirically motivated matching radius of 1 pixel in order to maximize the number of matches for a minimal number of chance superpositions.

We used the IRAF⁹ ApPhot/Phot tool for performing aperture photometry at the point-source locations for all IRAC bands and the MIPS $24\,\mu\text{m}$ band. For the four IRAC bands, we use an extraction aperture of $2''.4$, a local background annulus of $2''.4 - 7''.2$, and aperture corrections of 1.213, 1.234, 1.379, and 1.584 respectively. For the MIPS $24\,\mu\text{m}$ band, we use an extraction aperture of $3''.5$, a local background annulus of $6'' - 8''$, and an aperture correction of 2.78. We estimate the local background using a 2σ outlier rejection procedure in order to exclude sources located in the local sky annulus, and correct for the excluded pixels assuming a Gaussian background distribution. Using a background annulus immediately next to the signal aperture minimizes the effects of background variations in the crowded fields of the galaxies. We also determine the 3σ flux upper limit for each aperture location using the local background estimate.

Ideally, flux measurements of an isolated point source through either aperture or PSF photometry would produce the same results after appropriate aperture corrections (in the first case) and small zero-point offsets (in the second case) to account for flux underestimation due to PSF fitting up to finite radius rather than to infinity. We derive this small (usually ~ 0.1 mag) offset for each image from the mean difference between the magnitudes of relatively isolated, unsaturated bright sources measured through aperture and PSF photometry. For fainter sources, especially in limited spatial resolution images of crowded fields, the aperture and PSF photometry measurements can vary significantly. Figure 3 shows the differences between apparent magnitudes determined through aperture and PSF photometry as a function of PSF magnitude for the $m_{psf} < 15$ sources in NGC 6822 and M 81. For the less crowded case of NGC 6822, the two measurements generally agree for the very brightest sources in all four IRAC bands, with the scatter increasing for the fainter sources. The same is true for the $3.6\,\mu\text{m}$ and $4.5\,\mu\text{m}$ images of M 81, but at $5.8\,\mu\text{m}$, the scatter is much worse, although a sequence of bright sources with good agreement between the two sets of measurements can still be seen. However, for $8.0\,\mu\text{m}$, such a sequence cannot be clearly identified. We found this to be true for the other galaxies and M 81 shows behavior that is representative of all the targets apart from NGC 6822. Mismatches between the two magnitudes are a good indicator of when crowding is significantly effecting the magnitude estimates, and in the catalogs we list the difference between the PSF and aperture photometry magnitudes for each source.

⁹IRAF is distributed by the National Optical Astronomy Observatory, which is operated by the Association of Universities for Research in Astronomy (AURA) under cooperative agreement with the National Science Foundation.

Because of these crowding problems, we do not attempt to fine tune the $8.0\,\mu\text{m}$ PSF photometry measurements by applying the small linear offset, although we do this for the other three IRAC bands. For all IRAC bands, we universally prefer PSF photometry over aperture photometry, because PSF fitting is more successful at extracting relatively fainter sources in crowded fields. By definition, the nature of PSF fitting is that it takes into account whether the flux distribution of a potential point source is consistent with the PSF shape, and the degree of agreement or disagreement is reflected by a smaller or larger photometric uncertainty. Rather than conducting a bulk accounting of all excess flux within an aperture, PSF fitting measures a weighted sum of excess flux within a finite aperture. This is significant for fainter sources in crowded fields that are often close to brighter sources. PSF fitting more accurately identifies the flux associated with such sources isolating the contamination from other sources as well as more accurately subtracting the local sky. On the other hand, aperture photometry can significantly over subtract the sky and underestimate the source flux, or overestimate the source flux by failing to remove contamination from nearby brighter sources. Nevertheless, aperture photometry proves very useful for validating the PSF photometry measurements at the bright end in all IRAC bands, for estimating $5.8\,\mu\text{m}$ and $8.0\,\mu\text{m}$ fluxes where PSF fitting fails and $24\,\mu\text{m}$ flux where the lower resolution makes PSF photometry infeasible, and for determining flux upper limits.

To summarize, we implement strict detection criteria by requiring a $> 3\sigma$ detection of all cataloged sources at $3.6\,\mu\text{m}$ and $4.5\,\mu\text{m}$. We then complement those measurements at the $5.8\,\mu\text{m}$, $8.0\,\mu\text{m}$ and $24\,\mu\text{m}$ bands through a combination of PSF and aperture photometry, preferring PSF fitting over aperture photometry at $5.8\,\mu\text{m}$ and $8.0\,\mu\text{m}$, and exclusively using aperture photometry at $24\,\mu\text{m}$. For all objects that do not have a $> 3\sigma$ detection at these three longer wavelengths, we estimate 3σ flux upper limits.

3. Catalogs

In this Section, we discuss the results of our mid-IR photometric survey. Because we required a $> 3\sigma$ detection for each source at $3.6\,\mu\text{m}$ and $4.5\,\mu\text{m}$, the effective survey area for each galaxy is the overlap of the IRAC $3.6\,\mu\text{m}$ and $4.5\,\mu\text{m}$ image mosaics. Table 1 lists the effective survey area, gas phase ($\text{H}\alpha$) star formation rates adopted from Khan et al. (2013) and the number of point sources cataloged in each galaxy followed by the number of matches at < 0.5 and $0.5 - 1.0$ pixel, duplicates between the $3.6\,\mu\text{m}$ and $4.5\,\mu\text{m}$ source lists, and the number of $> 3\sigma$ counterparts identified at the three longer wavelength images for each galaxy. Tables 2 – 8 list the coordinates (J2000.0; RA and Dec) of the point sources followed by their Vega calibrated apparent magnitudes (m_λ), the associated 1σ uncertainties (σ_λ), and (for the $3.6 - 8.0\,\mu\text{m}$ bands) the differences between the PSF and aperture photometry magnitudes (δ_λ). For the $5.8\,\mu\text{m}$, $8.0\,\mu\text{m}$ and $24\,\mu\text{m}$ bands, $\sigma_\lambda = 99.99$ implies that the associated photometric measurement is a 3σ flux upper limit, and $m_\lambda = 99.99$ (as well as $\sigma_\lambda = 99.99$) indicates that no reliable photometric measurement could be obtained for that location. For the IRAC bands, $\delta_\lambda = 99.99$ implies that one or both of the associated photometric

measurements did not yield a $> 3\sigma$ flux measurement.

Figures 4 and 5 present the $m_{4.5}$ vs. $m_{3.6} - m_{4.5}$, $m_{5.8}$ vs. $m_{4.5} - m_{5.8}$, and $m_{8.0}$ vs. $m_{5.8} - m_{8.0}$ color magnitude diagrams (CMDs) for each galaxy. For comparison, we include the mid-IR CMDs for all sources in a 6 deg^2 region (see Khan et al. 2013, for details) of the NOAO Bootes Field produced from the *Spitzer* Deep Wide Field Survey (SDWFS, Ashby et al. 2009) data. Our catalogs simply inventory all the sources present on the image mosaics and do not attempt to distinguish between sources actually associated with the galaxies and unrelated contaminants. The contamination is significant for galaxies like NGC 247, which is highly inclined and covers a smaller fraction of the *Spitzer* images, than for the larger and more face-on galaxies (see Figure 1). Indeed, the CMDs of NGC 247 (Figure 5, second column) clearly show two distinct population of sources, with the break appearing near $m_{4.5} \simeq 18$. The CMDs of the two closest galaxies (NGC 6822 and M33) show distinguishable sequences of bright and red AGB stars (near $m_{4.5} \simeq 15$), but for the more distant galaxies this feature is less prominent (see Khan et al. 2010 for relevant discussion). The CMDs of NGC 7793 has the fewest identified point sources both due to its lower mass and because of poorer quality (more systematic artifacts) of its image mosaics.

Figure 6 show the apparent magnitude histograms of all sources in the catalog, with the shaded regions showing the sources in M33. It is apparent that the M33 catalog is $\sim 0.5 \text{ mag}$ shallower than the other catalogs in all bands. Overall, our source lists become significantly incomplete at $m_{3.6} \gtrsim 18$, $m_{4.5} \gtrsim 18$, $m_{5.8} \gtrsim 17$ and $m_{8.0} \gtrsim 16$. Figure 7 show the mid-IR color histograms of all sources in the catalog, with the shaded regions showing the sources with 1σ uncertainty in color $\lesssim 0.2$. It demonstrates the absence of any surprises in the color distributions and that the mid-color distributions are not due to large uncertainties. All normal stars have the same mid-IR color in the first two IRAC bands, because of the Rayleigh-Jeans tails of their spectra, and we see this from the sharp peak of color distribution at $m_{3.6} - m_{4.5} \simeq 0$. The longer wavelength detections are increasingly dominated by dusty stars, with color distribution peaks at $m_{3.6} - m_{5.8} = m_{4.5} - m_{5.8} \simeq 1$, $m_{3.6} - m_{8.0} = m_{4.5} - m_{8.0} \simeq 2$, and $m_{5.8} - m_{8.0} \simeq 1$. Figures 6 and 7 also show the apparent magnitude and color histograms of the SDWFS point sources (dotted lines). They show that our catalogs are $> 1 \text{ mag}$ deeper than the SDWFS catalog and the mid-IR color distribution of blank-field extragalactic sources significantly differs from that of fields containing nearby galaxies. In particular, at longer wavelengths, the galaxies contain more red sources (dusty stars) while the random extragalactic field sources are generally bluer.

Although we report the $24 \mu\text{m}$ photometry in the catalogs, these measurements have limited utility due to the lower spatial resolution of this band. The aperture used for this band commonly includes objects other than the intended target and is contaminated by emission from cold interstellar dust. Nevertheless, as we showed in Figure 5 of Khan et al. (2013), the spectral energy distributions of the normal stars show the expected negative slope for the Rayleigh-Jeans tail of their SEDs between $8 \mu\text{m}$ and $24 \mu\text{m}$. The $24 \mu\text{m}$ photometry can be very useful in specific cases, such as for studying evolved massive stars (see Khan et al. 2015, for details), despite the resolution limitation.

Where Thompson et al. (2009) identified $\sim 53,200$ sources in M33, and Khan et al. (2010) identified $\sim 11,200$ sources in NGC 300 and $\sim 6,000$ sources in M81, now we catalog $\sim 78,800$, $\sim 21,700$ and $\sim 28,600$ sources in these galaxies respectively. This is due to a number of factors. First, both of the earlier studies only cataloged the central regions of these galaxies, while here we analyze the full mosaics. Second, we use a larger matching radius of 1 pixel (rather than 0.5 pixel) to define point sources and a higher fraction of our cataloged sources can be coincidental matches between the $3.6\,\mu\text{m}$ and $4.5\,\mu\text{m}$. Third, the catalogs presented here are deeper due to improved photometry and search methods based on lessons learned from Khan et al. (2011, 2013, 2015). For example, Thompson et al. (2009) noted that their M33 point-source list becomes incomplete at $m_{3.6} = m_{4.5} > 17.1$, while we reach ~ 0.5 mag deeper for this galaxy and ~ 1 mag deeper for the rest.

We have compared our M33, NGC 300 and M81 catalogs with the $3.6\,\mu\text{m}$ and $4.5\,\mu\text{m}$ catalogs published by Thompson et al. (2009) and Khan et al. (2010). The photometric measurements at these two bands agree within the stated uncertainties for the brighter sources, with the scatter increasing towards the fainter sources. As is apparent from Figure 8, we identify zero point linear offsets between the older catalogs and the measurements reported here due to calibration differences. Thompson et al. (2009) performed PSF-fitting photometry and then converted the measurements to Vega-calibrated magnitudes using simple flux zero point shifts derived from aperture photometry flux measurements of 10 – 20 bright and isolated stars in each band. On the other hand, in this work as well as in Khan et al. (2010), we perform the PSF and aperture photometry measurements independently and then convert both to Vega-calibrated magnitudes using the flux zero points provided in the *Spitzer* Data Analysis Cookbook. This appears to have led to the ~ 0.2 magnitude linear zero-point offset between the Thompson et al. (2009) calibrations and our measurements for M33.

The more subtle offset between the Khan et al. (2010) calibrations and the measurements we report here for NGC 300 and M81 are due to the earlier work having used a background annulus far from the aperture ($1''.5$ aperture, $9'' - 15''$ annulus) to measure the local sky brightness when performing aperture photometry, whereas in this work we use a background annulus immediately adjacent to the aperture ($2''.4$ aperture, $2''.4 - 7''.2$ annulus). In a crowded field, where a source is likely to be contaminated by flux from adjacent sources, an annulus far from the aperture can underestimate the local sky. As the aperture photometry measurement is used to fine tune the PSF photometry to account for PSF fitting up to a finite radius rather than to infinity, this appears to have caused the < 0.1 magnitude offset. We identified this issue previously and adopted the current practice of using a background annulus immediately adjacent to the aperture (Khan et al. 2013, 2015).

Point-source catalogs of the inherently crowded galaxy fields that we are surveying are bound to be crowding limited, not just magnitude limited. While Figure 7 empirically demonstrates that our source detection peaks at a certain magnitude and then falls off rapidly, it is likely that incompleteness is affecting even the bright-star counts, increasing towards and through the peak. For

example, Martinez-Manso et al. (2015) suggests that even in a sparse field, incompleteness at the 5σ detection level can be on the order of 15%. Ideally, performing an artificial star completeness test through addition of randomly distributed artificial objects in the images could be useful.

However, the mid-IR bright stars (massive stars) are not randomly distributed, but in fact are highly clustered. Performing an efficiency determination test through addition of randomly distributed artificial objects in the images therefore would lead us to either overestimate or underestimate the efficiency. For such a study to be truly useful, it would require a proper “star-star correlation function” to be employed for spatial distribution of artificial stars. A star-star correlation function can also characterize the typical scale of the star clusters in each galaxy as a function of magnitude, to investigate the possible affect of aliasing. Such detailed modeling of source distribution is beyond the scope of the current paper and we encourage future studies to explore this issue.

This catalog is a resource as an archive for studying mid-IR transients and for planning observations with the James Webb Space Telescope. Our survey is being expanded to galaxies with $\sim 10\times$ higher integrated star formation rate than for these seven galaxies. While we have shown that surveys for stellar populations are feasible using archival Spitzer data, JWST will be a far more powerful probe of stars in the mid-IR. The nearly order-of-magnitude higher resolution (Gardner et al. 2006) of JWST compared to *Spitzer* can be used either to greatly reduce the problem of confusion in these galaxies or to greatly expand the survey volume.

We would like to thank the referee for providing helpful feedback. This work is based on observations made with the *Spitzer* Space Telescope, which is operated by the Jet Propulsion Laboratory, California Institute of Technology under a contract with the National Aeronautics and Space Administration (NASA). We extend our gratitude to the SINGS Legacy Survey and the LVL Survey for making their data publicly available. RK is supported through a JWST Fellowship hosted by the Goddard Space Flight Center and awarded as part of the NASA Postdoctoral Program operated by the Oak Ridge Associated Universities on behalf of NASA.

REFERENCES

- Ashby, M. L. N. et al. 2009, ApJ, 701, 428
- Barmby, P. et al. 2006, ApJ Letters, 650, L45
- Benjamin, R. A. et al. 2003, PASP, 115, 953
- Bolatto, A. D., Simon, J. D., Stanimirović, S., et al. 2007, ApJ, 655, 212
- Bonanos, A. Z. et al. 2006, ApJ, 652, 313
- Dale, D. A. et al. 2009, ApJ, 703, 517

- Fazio, G. G. et al. 2004, *ApJS*, 154, 10
- Gardner, J. P. et al. 2006, *Space Sci. Rev.*, 123, 485
- Gerke, J. R. & Kochanek, C. S. 2013, *ApJ*, 762, 64
- Gerke, J. R., Kochanek, C. S., Prieto, J. L., Stanek, K. Z., & Macri, L. M. 2011, *ApJ*, 743, 176
- Gieren, W. et al. 2005, *ApJ*, 628, 695
- . 2006, *ApJ*, 647, 1056
- Gordon, K. D., Meixner, M., Meade, M. R., et al. 2011, *AJ*, 142, 102
- Helou, G., Roussel, H., Appleton, P., et al. 2004, *ApJS*, 154, 253
- Kennicutt, Jr., R. C. et al. 2003, *PASP*, 115, 928
- Khan, R., Kochanek, C. S., Stanek, K. Z., & Gerke, J. 2015, *ApJ*
- Khan, R., Stanek, K. Z., & Kochanek, C. S. 2013, *ApJ*, 767, 52
- Khan, R., Stanek, K. Z., Kochanek, C. S., & Bonanos, A. Z. 2011, *ApJ*, 732, 43
- Khan, R., Stanek, K. Z., Prieto, J. L., Kochanek, C. S., Thompson, T. A., & Beacom, J. F. 2010, *ApJ*, 715, 1094
- Madore, B. F., Freedman, W. L., Catanzarite, J., & Navarrete, M. 2009, *ApJ*, 694, 1237
- Martinez-Manso, J., Gonzalez, A. H., Ashby, M. L. N., et al. 2015, *MNRAS*, 446, 169
- McQuinn, K. B. W. et al. 2007, *ApJ*, 664, 850
- Meixner, M. et al. 2006, *AJ*, 132, 2268
- Mould, J., Barmby, P., Gordon, K., et al. 2008, *ApJ*, 687, 230
- Rieke, G. H. et al. 2004, *ApJS*, 154, 25
- Saha, A. et al. 2006, *ApJS*, 165, 108
- Sheth, K. et al. 2008, in *Spitzer Proposal ID #60007*, 60007
- Stetson, P. B. 1992, 25, 297
- Thompson, T. A., Prieto, J. L., Stanek, K. Z., Kistler, M. D., Beacom, J. F., & Kochanek, C. S. 2009, *ApJ*, 705, 1364
- Tully, R. B., Rizzi, L., Shaya, E. J., Courtois, H. M., Makarov, D. I., & Jacobs, B. A. 2009, *AJ*, 138, 323

Werner, M. W. et al. 2004, ApJS, 154, 1

Willner, S. P., Ashby, M. L. N., Barmby, P., et al. 2004, ApJS, 154, 222

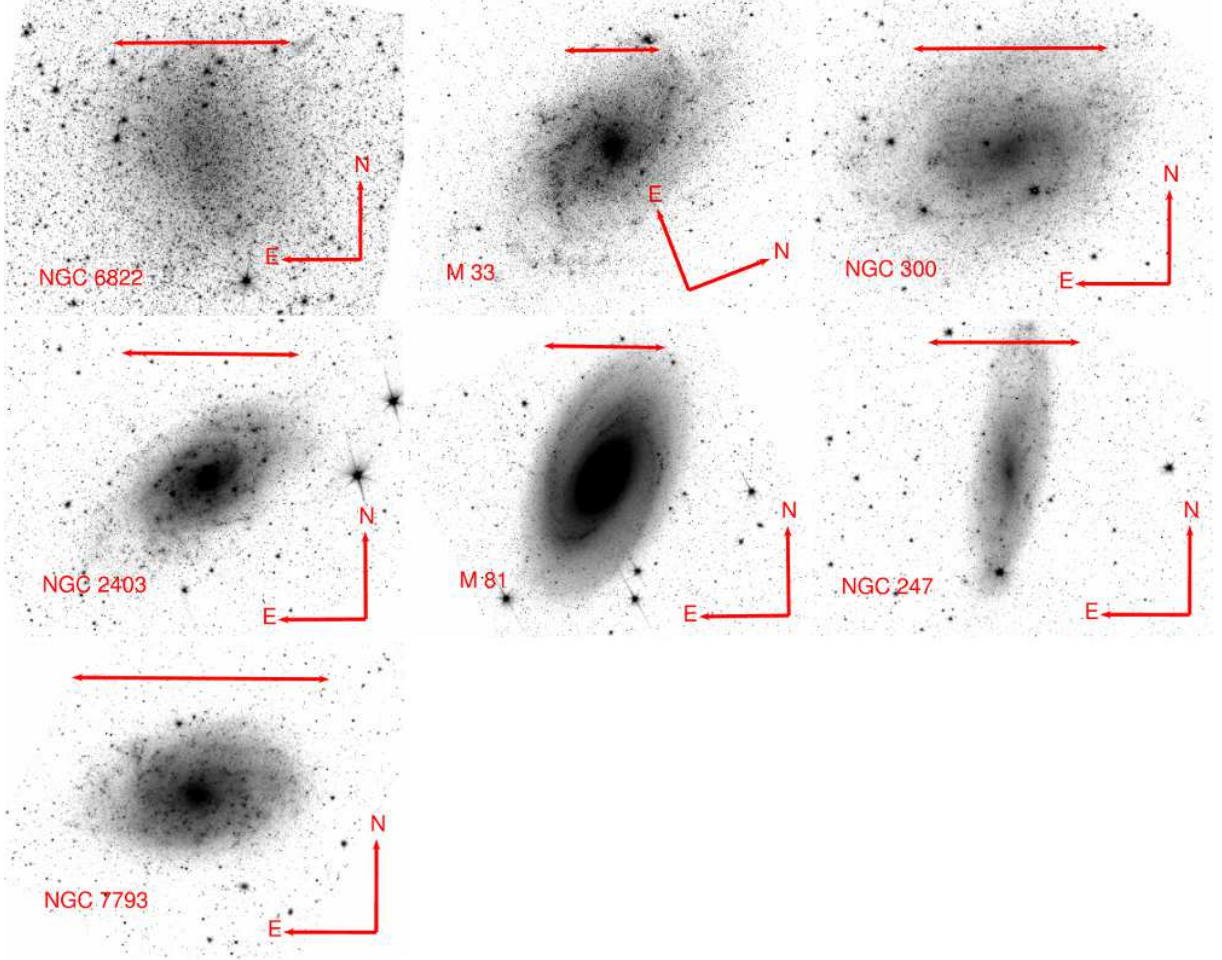


Fig. 1.— The IRAC $3.6\,\mu\text{m}$ images of the seven targeted galaxies: NGC 6822, M 33, NGC 300, NGC 2403, M 81, NGC 247, and NGC 7793. The red line on each figure spans $10'$.

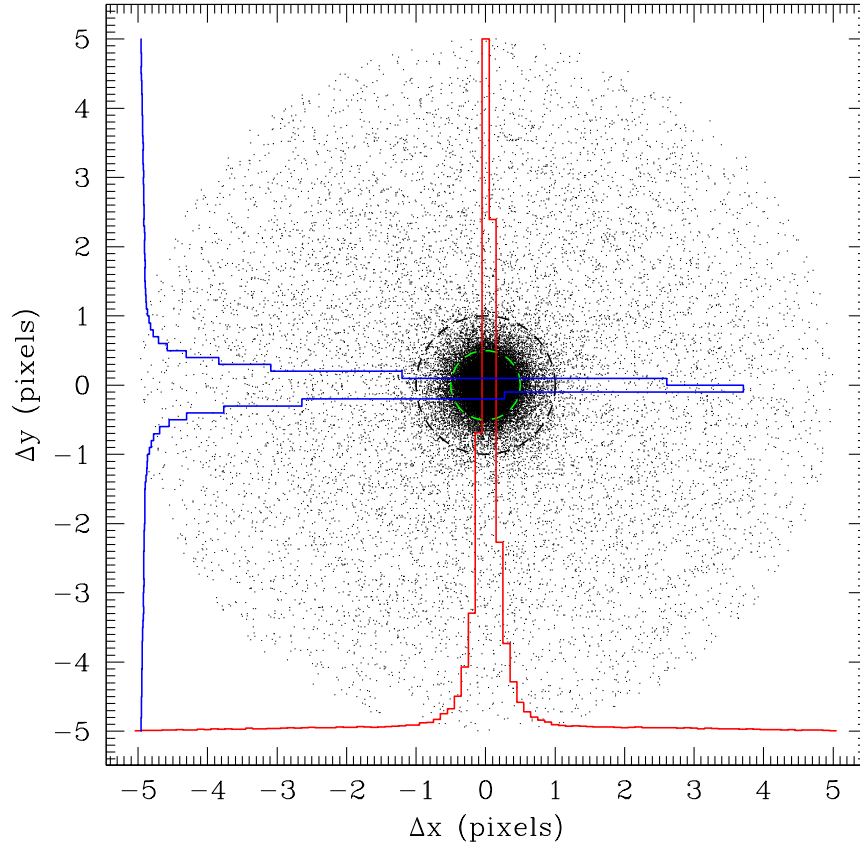


Fig. 2.— The distances (in pixels) to the nearest $3.6\,\mu\text{m}$ source for each $4.5\,\mu\text{m}$ source in M33 along the x axis (Δx) and y axis (Δy) of the images. The blue and red histograms show the distance distributions. The radius of the concentric circles are 0.5 pixel (green) and 1 pixel (black). In this case, most sources ($> 90\%$) have a match within 0.5 pixels, and the density of nearest matches falls rapidly between 0.5 – 1.0 pixel ($< 10\%$ additional matches) while the number of duplicate matches increase ($< 0.5\%$ duplicate matches). At larger distances, the distribution essentially flattens. Similar distributions are observed for the other six galaxies (see Table 1).

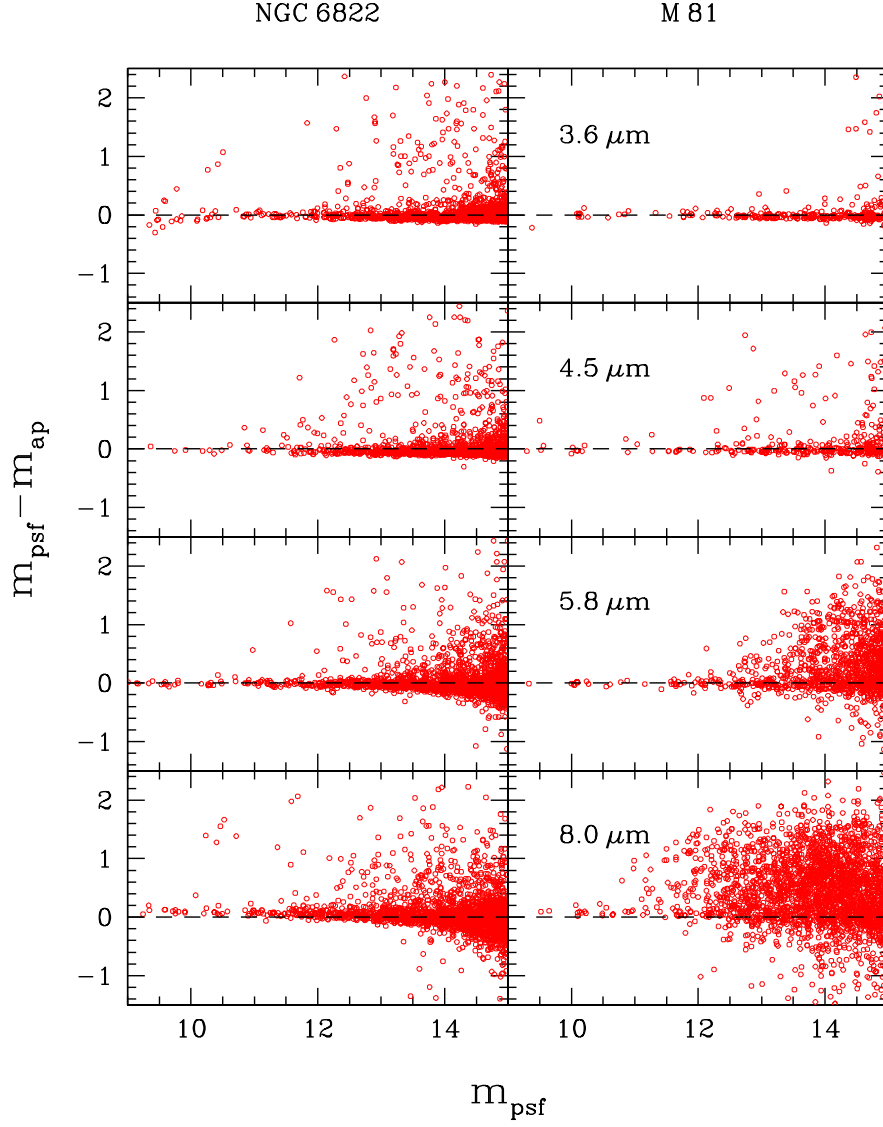


Fig. 3.— The differences between aperture and PSF photometry magnitudes as a function of the PSF magnitudes for the $m_{\text{psf}} < 15$ sources in NGC 6822 and M 81. For the less crowded case of NGC 6822, the two measurements generally agree in all four IRAC bands, with the scatter increasing for the fainter sources. The same is true for the 3.6 μm and 4.5 μm images of M 81, but at 5.8 μm , the scatter increases rapidly, and for 8.0 μm the situation worsens further. We found this to be true for the other galaxies and M 81 shows behavior that is representative of all the targets apart from NGC 6822.

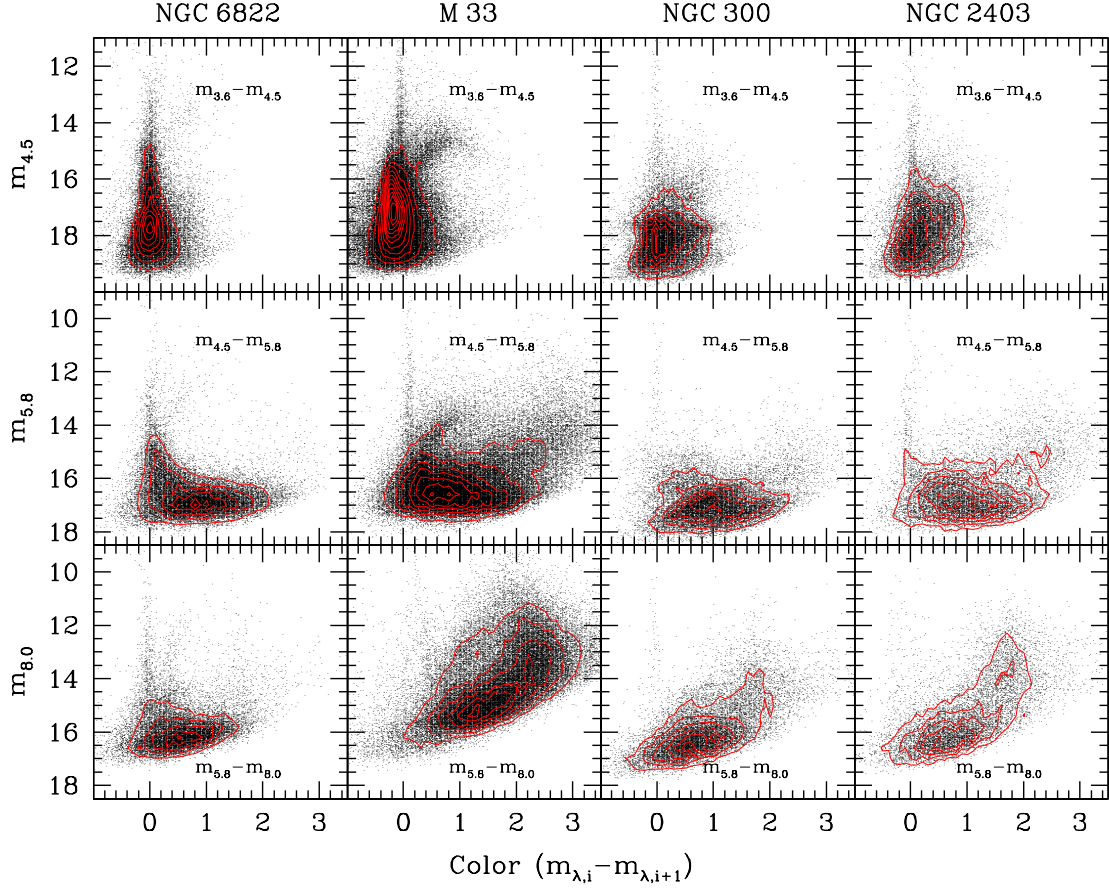


Fig. 4.— The $m_{4.5}$ vs. $m_{3.6} - m_{4.5}$ (top row), $m_{5.8}$ vs. $m_{4.5} - m_{5.8}$ (middle row), and $m_{8.0}$ vs. $m_{5.8} - m_{8.0}$ (bottom row) color magnitude diagrams (CMDs) for the $> 3\sigma$ sources in NGC 6822, M 33, NGC 300 and NGC 2403. The red lines represent isodensity contours.

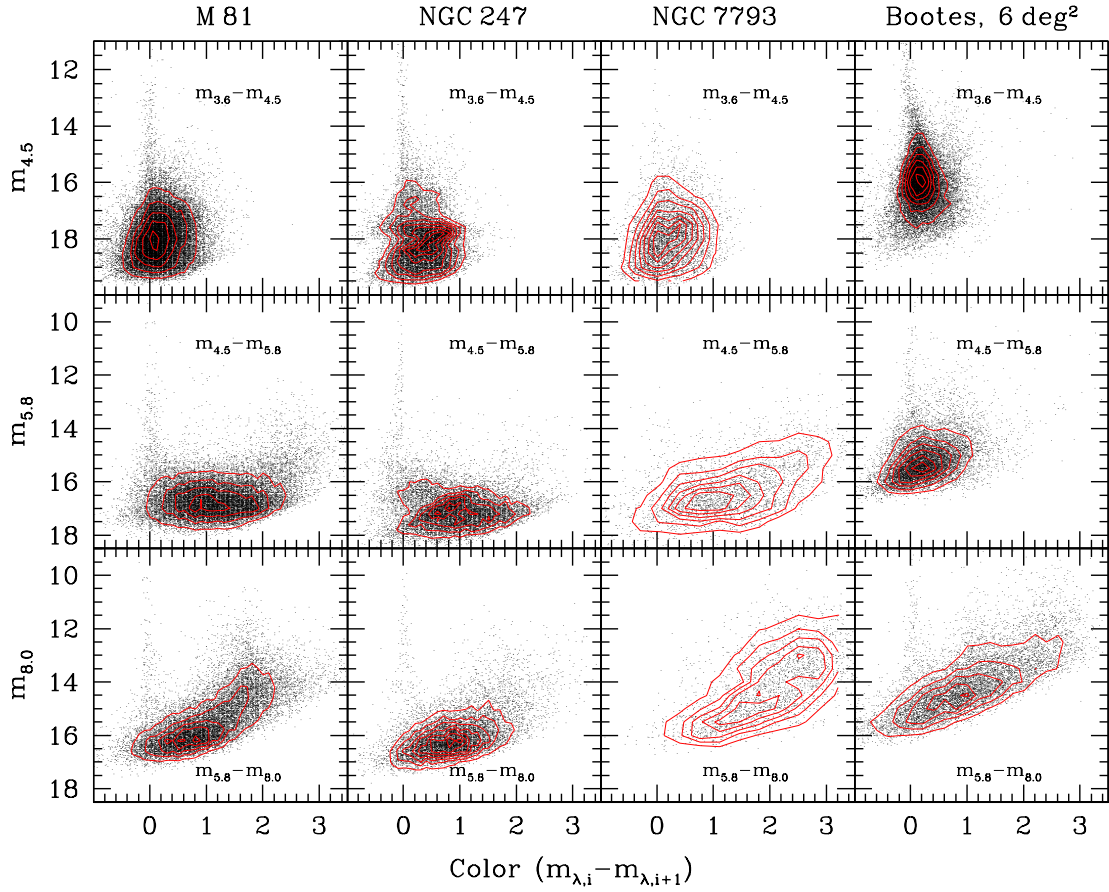


Fig. 5.— Same as Figure 4, but for the galaxies M 81, NGC 247, NGC 7793, and (for comparison) a 6 deg² region of the NOAO Bootes Field from the *Spitzer* Deep Wide Field Survey (SDWFS, Ashby et al. 2009) data.

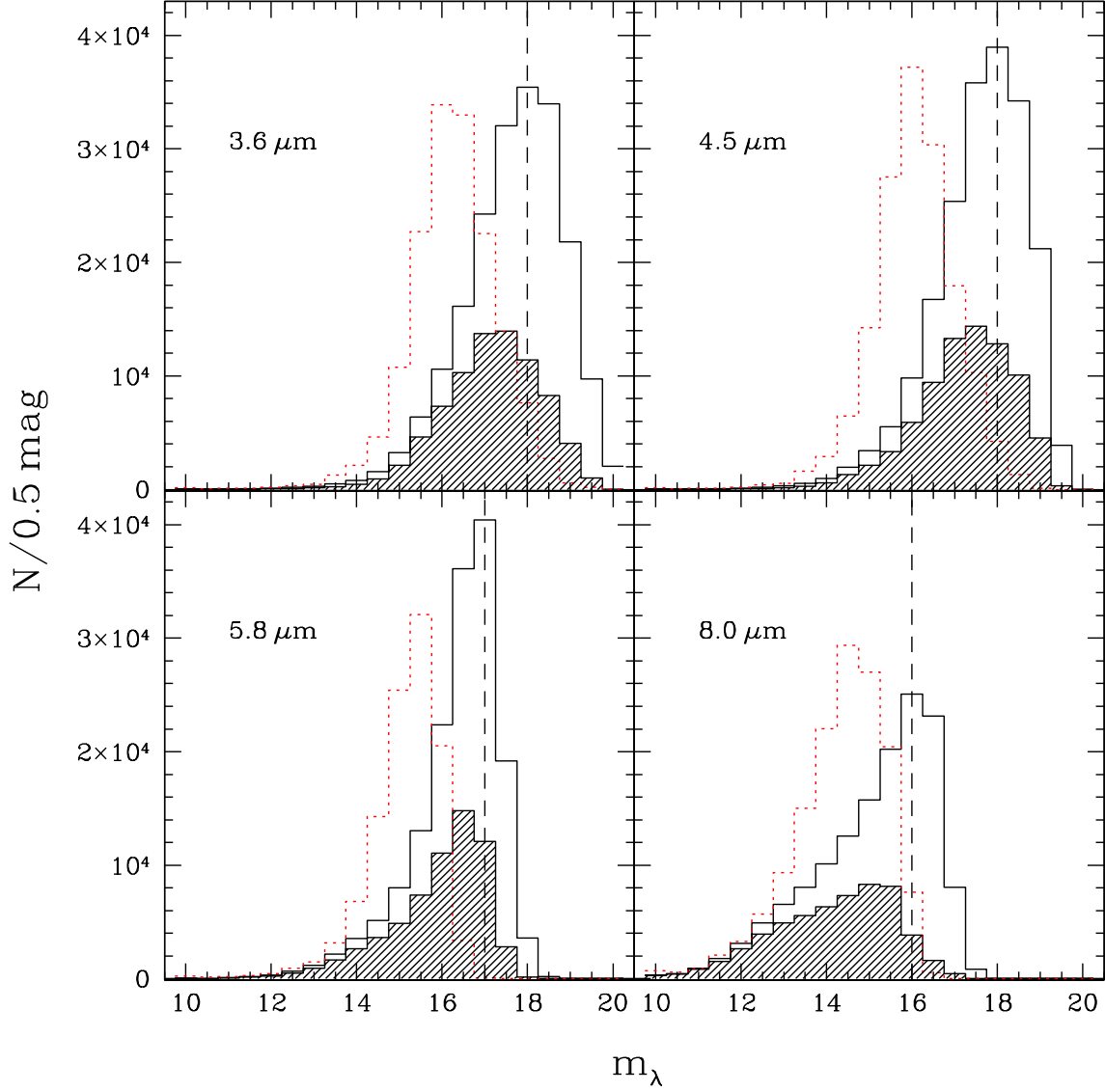


Fig. 6.— Apparent magnitude histograms for all the sources in the catalog, with the shaded regions showing the sources in M33. Overall, the source lists become incomplete at (locations marked by the dashed vertical lines) $m_{3.6} \gtrsim 18$, $m_{4.5} \gtrsim 18$, $m_{5.8} \gtrsim 17$ and $m_{8.0} \gtrsim 16$. The M33 source list is roughly ~ 0.5 mag shallower than for the other galaxies. The dotted lines show the apparent-magnitude histograms of the SDWFS catalog sources, scaled up for clarity by a factor of 7 for $m_{3.6}$ and $m_{4.5}$, and by a factor of 10 for $m_{5.8}$ and $m_{8.0}$.

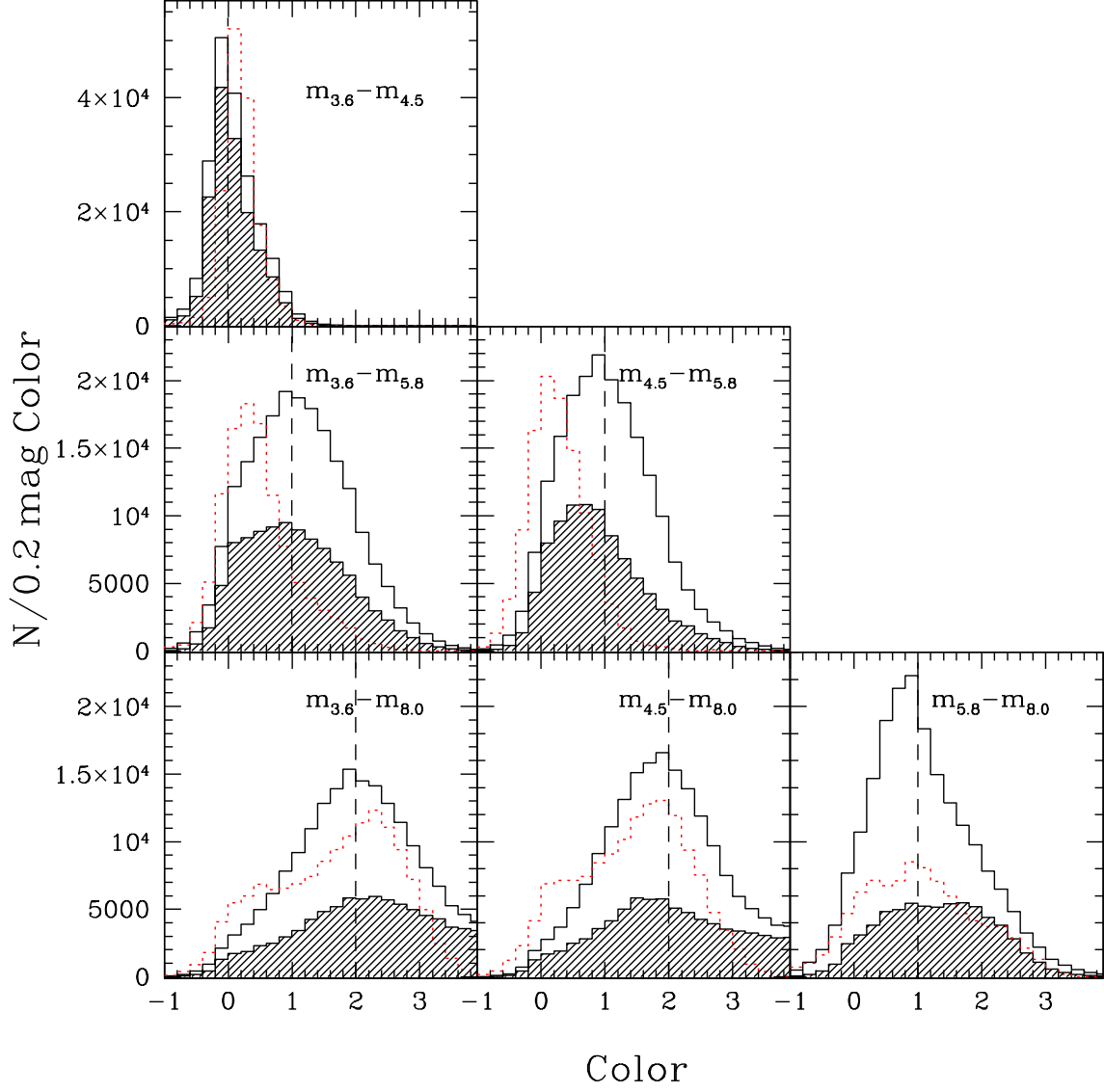


Fig. 7.— Mid-IR color histograms for all the sources in the catalog, with the shaded histograms showing the distribution of sources with 1σ uncertainty in color $\lesssim 0.2$. The sharp peak of color distribution at $m_{3.6} - m_{4.5} \simeq 0$ is due to the Rayleigh-Jeans tail of the spectra of all normal stars. The longer wavelengths are increasingly dominated by dusty stars, with color distribution peaks at (locations marked by the dashed vertical lines) $m_{3.6} - m_{5.8} = m_{4.5} - m_{5.8} \simeq 1$, $m_{3.6} - m_{8.0} = m_{4.5} - m_{8.0} \simeq 2$, and $m_{5.8} - m_{8.0} \simeq 1$. The dotted lines show the mid-IR color histograms of the SDWFS catalog sources, scaled-up for clarity by a factor of 7 for $m_{3.6} - m_{4.5}$, and a factor of 10 for the rest..

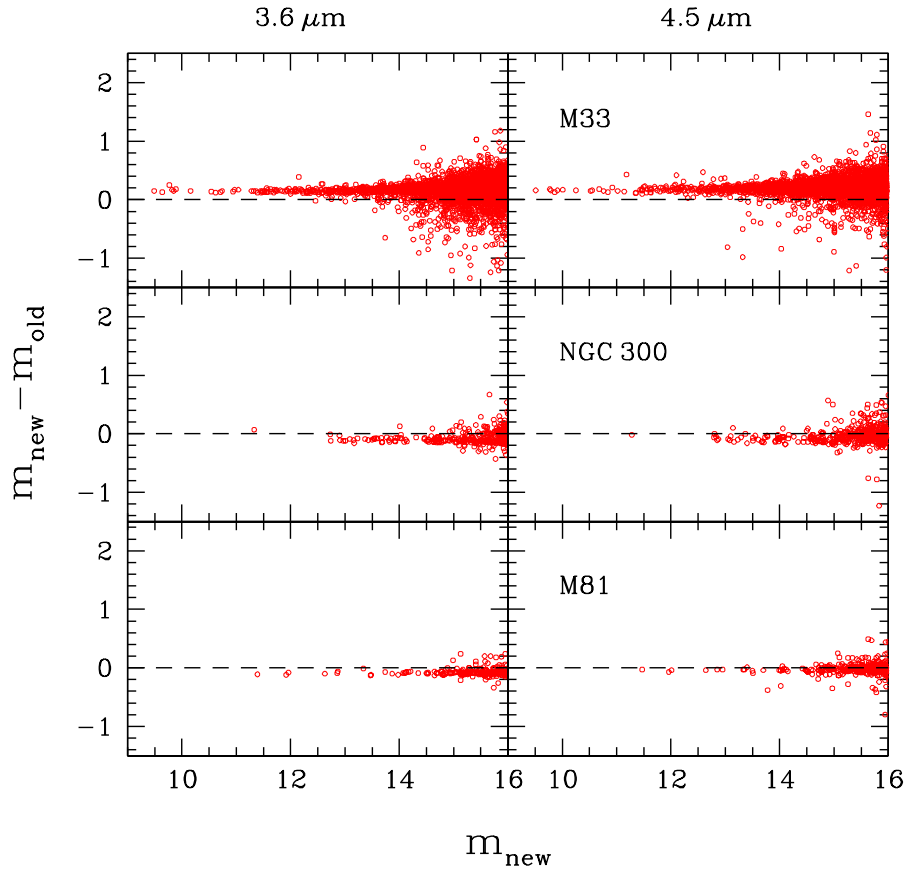


Fig. 8.— The differences between $3.6\,\mu\text{m}$ and $4.5\,\mu\text{m}$ magnitudes reported by Thompson et al. (2009) for M33 and by Khan et al. (2010) for NGC 300 and M81 (m_{old}) as compared to our measurements at those bands for the same sources (m_{new}). Aside from the linear offsets due to calibration differences, as discussed in Section 3, the photometric measurements at these two bands agree within the stated uncertainties for the brighter sources, with the scatter increasing towards the fainter sources.

Table 1: Catalog Statistics

	NGC 6822	M 33	NGC 300	NGC 2403	M 81	NGC 247	NGC 7793
Survey Area (deg ²)	~ 0.1	~ 0.73	~ 0.17	~ 0.12	~ 0.17	~ 0.2	~ 0.044
SFR ($M_{\odot}/year$)	0.01	0.33	0.11	0.44	0.46	0.17	0.33
Point Sources	30,745	78,841	21,739	17,022	28,674	16,658	5,617
Matched within < 0.5 pixel	24,134	71,439	16,209	12,563	18,383	12,741	3,401
Matched within 0.5 – 1.0 pixel	6,611	7,402	5,530	4,459	10,291	3,917	2,216
Duplicate Matches	142	271	64	87	66	39	54
> 3σ at $5.8\ \mu\text{m}$	23,906	62,974	18,043	12,712	21,332	13,893	3,389
> 3σ at $8.0\ \mu\text{m}$	20,414	56,145	17,204	12,113	20,069	11,995	4,018
> 3σ at $24\ \mu\text{m}$	7,268	23,004	7,322	6,886	11,557	5,297	2,478

Table 2: Catalog for 30,745 Point Sources in NGC 6822

RA (deg)	Dec (deg)	$m_{3.6}$ (mag)	$\sigma_{3.6}$	$\delta_{3.6}$	$m_{4.5}$ (mag)	$\sigma_{4.5}$	$\delta_{4.5}$	$m_{5.8}$ (mag)	$\sigma_{5.8}$	$\delta_{5.8}$	$m_{8.0}$ (mag)	$\sigma_{8.0}$	$\delta_{8.0}$	m_{24} (mag)	σ_{24}
...
296.37946	−14.74545	9.07	0.12	−0.22	8.94	0.10	−0.09	9.00	0.03	0.02	9.34	0.04	0.21	8.80	0.01
296.23211	−14.72759	9.34	0.11	−0.18	9.09	0.03	−0.08	9.14	0.02	0.00	9.24	0.04	0.05	9.13	0.02
296.31297	−14.77366	9.48	0.06	−0.07	9.35	0.05	0.10	9.16	0.04	−0.01	9.34	0.01	0.12	9.08	0.03
296.32372	−14.71925	9.46	0.03	−0.10	9.37	0.04	0.03	9.33	0.03	−0.01	9.59	0.04	0.13	9.30	0.02
296.13722	−14.94461	9.77	0.06	−0.01	9.39	0.07	−0.16	9.54	0.03	0.00	9.72	0.02	0.12	9.37	0.02
...

Table 3: Catalog for 78,841 Point Sources in M 33

RA (deg)	Dec (deg)	$m_{3.6}$ (mag)	$\sigma_{3.6}$	$\delta_{3.6}$	$m_{4.5}$ (mag)	$\sigma_{4.5}$	$\delta_{4.5}$	$m_{5.8}$ (mag)	$\sigma_{5.8}$	$\delta_{5.8}$	$m_{8.0}$ (mag)	$\sigma_{8.0}$	$\delta_{8.0}$	m_{24} (mag)	σ_{24}
...
23.40441	30.38922	7.72	0.05	-0.69	7.75	0.03	-0.20	7.66	0.02	0.04	7.60	0.06	0.01	7.65	0.05
23.66245	30.84435	7.86	0.03	-0.60	7.89	0.02	-0.15	7.74	0.01	0.02	7.65	0.11	0.01	7.69	0.01
23.82179	30.67099	8.14	0.04	-0.49	8.20	0.02	-0.10	8.13	0.01	0.05	8.02	0.10	-0.04	8.13	0.01
23.23681	30.26192	7.99	0.04	-0.85	8.54	0.03	-0.20	8.03	0.02	0.04	8.25	0.10	0.04	7.51	0.01
23.34689	30.94818	8.54	0.03	-0.24	9.25	0.03	0.04	8.39	0.01	0.03	8.97	0.08	-0.15	8.40	0.01
...

Table 4: Catalog for 21,739 Point Sources in NGC 300

RA (deg)	Dec (deg)	$m_{3.6}$ (mag)	$\sigma_{3.6}$	$\delta_{3.6}$	$m_{4.5}$ (mag)	$\sigma_{4.5}$	$\delta_{4.5}$	$m_{5.8}$ (mag)	$\sigma_{5.8}$	$\delta_{5.8}$	$m_{8.0}$ (mag)	$\sigma_{8.0}$	$\delta_{8.0}$	m_{24} (mag)	σ_{24}
...
13.45595	-37.68470	10.96	0.09	0.72	10.13	0.04	-0.03	10.19	0.01	0.04	10.20	0.01	0.11	10.11	0.03
13.87874	-37.65598	10.23	0.09	-0.05	10.31	0.04	0.08	10.19	0.03	0.02	10.28	0.02	0.08	9.97	0.02
13.62935	-37.77459	10.43	0.04	-0.11	10.54	0.04	0.01	10.57	0.01	0.03	10.62	0.02	0.10	10.58	0.05
13.74223	-37.51812	10.91	0.04	-0.06	10.99	0.02	-0.01	10.92	0.02	0.01	11.03	0.02	0.08	11.30	0.12
13.92891	-37.74328	11.09	0.05	0.02	11.11	0.03	0.01	11.06	0.02	0.02	11.18	0.02	0.09	11.03	0.10
...

Table 5: Catalog for 17,022 Point Sources in NGC 2403

RA (deg)	Dec (deg)	$m_{3.6}$ (mag)	$\sigma_{3.6}$	$\delta_{3.6}$	$m_{4.5}$ (mag)	$\sigma_{4.5}$	$\delta_{4.5}$	$m_{5.8}$ (mag)	$\sigma_{5.8}$	$\delta_{5.8}$	$m_{8.0}$ (mag)	$\sigma_{8.0}$	$\delta_{8.0}$	m_{24} (mag)	σ_{24}
...
114.26503	65.49629	9.88	0.04	-0.06	9.86	0.01	-0.06	9.89	0.02	-0.00	10.15	0.04	0.22	9.90	0.03
113.70299	65.56170	9.92	0.06	-0.09	10.00	0.02	-0.06	10.01	0.02	0.01	9.88	0.06	-0.18	9.93	0.05
114.20327	65.59495	10.17	0.06	-0.04	10.09	0.05	-0.07	10.18	0.05	-0.00	10.36	0.04	-0.08	8.87	0.20
114.04298	65.75131	10.43	0.07	0.00	10.41	0.08	-0.09	10.44	0.03	-0.02	10.27	0.06	-0.18	10.11	0.04
113.65425	65.53209	10.93	0.15	0.14	10.42	0.11	-0.07	10.86	0.14	0.18	10.44	0.04	-0.05	10.50	0.04
...

Table 6: Catalog for 28,674 Point Sources in M 81

RA (deg)	Dec (deg)	$m_{3.6}$ (mag)	$\sigma_{3.6}$	$\delta_{3.6}$	$m_{4.5}$ (mag)	$\sigma_{4.5}$	$\delta_{4.5}$	$m_{5.8}$ (mag)	$\sigma_{5.8}$	$\delta_{5.8}$	$m_{8.0}$ (mag)	$\sigma_{8.0}$	$\delta_{8.0}$	m_{24} (mag)	σ_{24}
...
148.36619	68.97859	9.38	0.06	-0.23	9.30	0.10	-0.03	9.33	0.02	-0.01	9.52	0.02	0.11	9.43	0.01
148.93766	69.02938	10.12	0.04	0.01	10.00	0.06	-0.07	10.04	0.03	-0.01	10.16	0.06	0.09	10.31	0.09
148.67614	69.09785	10.12	0.04	0.01	10.02	0.05	0.04	10.09	0.04	0.01	10.13	0.03	0.10	10.05	0.12
148.61902	69.22280	10.09	0.04	0.02	10.08	0.05	-0.01	10.00	0.03	0.00	10.10	0.06	0.09	9.92	0.02
148.81385	69.25521	10.14	0.03	0.02	10.10	0.03	-0.02	10.05	0.03	-0.03	10.10	0.04	0.02	10.13	0.03
...

